

IN VIVO TRANS-RECTAL ULTRASOUND-COUPLED NEAR-INFRARED OPTICAL TOMOGRAPHY OF INTACT NORMAL CANINE PROSTATE

DAQING PIAO^{*,†}, ZHEN JIANG[†], KENNETH E. BARTELS[‡],
G. REED HOLYOAK[‡], JERRY W. RITCHEY[§], GUAN XU[†],
CHARLES F. BUNTING[†] and GENNADY SLOBODOV[¶]

[†]*School of Electrical and Computer Engineering
Oklahoma State University, Stillwater, OK 74078 USA
daqing.piao@okstate.edu

[‡]*Department of Veterinary Clinical Sciences
Oklahoma State University, Stillwater, OK 74078 USA*

[§]*Department of Veterinary Pathobiology
Oklahoma State University, Stillwater, OK 74078 USA*

[¶]*Department of Urology, University of Oklahoma Health
Sciences Center, Oklahoma City, OK 73104 USA*

This is the first tomography-presentation of the optical properties of a normal canine prostate, *in vivo*, in its native intact environment in the pelvic canal. The imaging was performed by trans-rectal near-infrared (NIR) optical tomography in steady-state measurement at 840 nm on three sagittal planes across the right lobe, middle-line, and left lobe, respectively, of the prostate gland. The NIR imaging planes were position-correlated with concurrently applied trans-rectal ultrasound, albeit there was no spatial *prior* employed in the NIR tomography reconstruction. The reconstructed peak absorption coefficients of the prostate on the three planes were 0.014, 0.012, and 0.014 mm⁻¹. The peak reduced scattering coefficients were 5.28, 5.56, and 6.53 mm⁻¹. The peak effective attenuation coefficients were 0.45, 0.43, and 0.50 mm⁻¹. The absorption and effective attenuation coefficients were within the ranges predictable at 840 nm by literature values which clustered sparsely from 355 nm to 1064 nm, none of which were performed on a canine prostate with similar conditions. The effective attenuation coefficients of the gland were shown to be generally higher in the internal aspects than in the peripheral aspects, which is consistent with the previous findings that the urethral regions were statistically more attenuating than the capsular regions.

Keywords: Prostate; canine; optical property; optical tomography; trans-rectal ultrasound.

1. Introduction

The knowledge of tissue optical properties relevant to light diffusion or attenuation is important to both the dosimetry of photodynamic therapy (PDT)^{1–4} and the analysis based on near-infrared (NIR) diffuse optical imaging.^{5–10} The prostate of

the dog is usually considered as a model closest to that of the human being, therefore a number of studies have been conducted^{11–20} on canine subjects to estimate the optical properties of prostate, *in vitro* or *in vivo*, over a wide range of spectrum (to be reviewed in more detail in Sec. 2 of this

study). A general consensus that has been made from these studies is that significant intra-organ and inter-subject variations of the prostate optical properties do occur. The optical properties being investigated include the absorption coefficient, the reduced or transport scattering coefficient, and the effective attenuation coefficient that is a combination of the above two properties. The reported intra-organ and inter-subject prostate optical heterogeneity imposes the need of individualized and localized measurement for PDT applications,¹⁸ as well as challenges to trans-rectal NIR tomography that aims to resolve the optical contrast, either endogenous^{21,22} or exogenous,²³ of prostate cancerous lesions over normal or benign prostate tissues.

It is also important in PDT to know the optical properties of peri-prostatic tissues, such as rectal or peri-rectal regions since the existence of any optical property gradient of the prostate over its peripheral tissue will influence the local peri-prostatic light distribution. For trans-rectal NIR tomography of the prostate, the NIR light is attenuated first by a condom (required for endo-rectal application), then by the rectal wall and the peri-rectal tissue before finally reaching the prostate. The degree of NIR light propagation into the prostate is dependent upon the optical property gradients between the prostatic capsule and peri-prostatic tissue. The *in vivo* or *in vitro* optical contrast of the prostate with respect to peri-rectal or peri-prostatic tissue is therefore fundamental to PDT and prostate NIR tomography, yet to our knowledge it has rarely been evaluated on a single subject. Overall there is very limited information regarding the NIR attenuating features of peri-rectal tissue.¹¹ Therefore, it is difficult to draw a comparison of the optical properties reported in different studies between the prostate and the peri-rectal tissue. Except the current reported *in vivo* investigation, all of the studies on normal prostate (canine and human) have been taken interstitially on exposed prostate or through trans-perineal imaging. The interstitial measurements, although very reliable and consistent, are likely to alter to some extent the optical properties natural to the tissue being measured.

In this work we present tomographic measurements of optical properties of a normal canine prostate, *in vivo*, in its native intact environment in the pelvic canal. The imaging was performed by trans-rectal NIR optical tomography in steady-state measurement at 840 nm, on

three sagittal planes across the right lobe, middle-line, and left lobe, respectively, of the prostate gland. The NIR imaging planes were position-correlated with concurrently applied trans-rectal ultrasound, albeit there was no spatial *prior* employed in the NIR tomography reconstruction. The prostate gland appears as a positive-contrast region in NIR images, particularly in the absorption and effective-attenuation images. The position and profile of the positive-contrast prostate-indicating region correlate well with those of the prostate in the concurrent trans-rectal ultrasound image. The peak absorption coefficients of the prostate-region on the three planes were found to be 0.014, 0.012, and 0.014 mm⁻¹. The peak reduced scattering coefficients were 5.28, 5.56, and 6.53 mm⁻¹. The peak effective attenuation coefficients were 0.45, 0.43, and 0.50 mm⁻¹. The absorption and effective attenuation coefficients were within the ranges that are predictable at 840 nm based on literature values which clustered sparsely from 355 nm to 1064 nm, none of which were performed on a prostate in similar conditions. It is also noted that effective attenuation coefficients of the gland are higher in the internal aspect than in the peripheral aspect, which is consistent with the previous findings of statistically more attenuating urethral regions than the capsular regions.








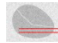

2. Review of the Optical Property Measurements on Canine Prostate

Tables 1 and 2 summarize what the authors have found to be existing methods, represented graphically by diagram (Table 1), and published values (Table 2) on optical properties of the canine prostate within the spectral range from 355 nm to 1064 nm. In Table 2, the attenuation coefficient is denoted by μ_a , the reduced scattering coefficient by μ'_s , and the effective attenuation coefficient by μ_{eff} that is defined as

$$\mu_{\text{eff}} = \sqrt{3\mu_a(\mu_a + \mu'_s)}. \quad (1)$$

Oraevsky *et al.* presented *in vitro* μ_a , μ'_s , and μ_{eff} of prostate at 355, 532, and 1064 nm, respectively, using opto-acoustic time-resolved fluence rate measurements on slab samples of normal canine prostate tissues.¹² Another post-mortem study by Chen *et al.* estimated prostate μ_a , μ'_s , and μ_{eff} at 630 nm, by interstitial measurements on excised

Table 1. Legend indicating the measurement methods used in Table 2.

								
Opto-acoustic on slab tissue	Integrating sphere on slab tissue	Interstitial on exposed prostate	Interstitial on excised prostate	Reflective on exposed prostate	Interstitial close to the capsule	Interstitial close to the urethra	Interstitial close to the base	Interstitial close to the apex

normal prostate.¹³ *In vitro* μ_a and μ'_s of slab samples of normal canine prostate tissues were evaluated at 633 nm, by employing steady-state fluence rate measurements using the standard double-integrating sphere technique.¹⁵ Other studies relied on steady-state fluence rate measurements on tissues *in situ*, albeit involving surgical procedures to expose the prostatic tissue to the fiber, to determine μ_{eff} of the normal canine prostate. At wavelengths of 630, 665, 730, 732 nm, interstitial measurements on normal canine prostate *in vivo* were conducted before and after PDT.^{14,17,18,20} Perhaps the only *in vivo* study using reflection measurement upon exposed prostate, thereby maintaining the intactness of the gland itself, was performed at 732 nm on exposed normal canine prostate.¹⁹ Trans-perineal interstitial measurement,^{16–18} which in principle is more accurate than interstitial measurement on exposed prostate, demonstrated with statistical significance that the μ_{eff} of prostatic urethral regions is higher than that of the prostatic capsular regions.^{16,17}

In Table 2, there are some individual values of μ_a and μ'_s , but nevertheless most original values listed are regarding μ_{eff} only, which are readily available from steady-state fluence rate measurements. Because the data are clustered in a wide spectrum, summarizing all these studies to a single category for spectrally-resolved comparative evaluation can only be made by utilizing μ_{eff} since it represents the coupled effect of μ_a and μ'_s . When the standard deviations of μ_a and μ'_s , denoted by $\sigma\mu_a$ and $\sigma\mu'_s$, respectively, are available, the standard deviation of μ_{eff} in Table 2 is calculated based on Eq. (1) by

$$\sigma\mu_{\text{eff}} = \sqrt{\left(\frac{\partial\mu_{\text{eff}}}{\partial\mu_a}\sigma\mu_a\right)^2 + \left(\frac{\partial\mu_{\text{eff}}}{\partial\mu'_s}\sigma\mu'_s\right)^2}. \quad (2)$$

3. Methods and Materials


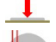

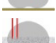






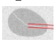












3.1. Trans-rectal US-coupled NIR tomography

The details of the trans-rectal US-coupled NIR tomography system can be found elsewhere.^{21,22}

Figure 1 illustrates the configuration of the trans-rectal NIR/US probe and the prostate imaging geometry. Since NIR imaging depth is typically $1/2$ of the array dimension, the NIR optodes are distributed longitudinally in parallel to the sagittal US to allow interrogating deep prostatic tissues. The NIR arrays are also put symmetrically on the lateral sides of the sagittal US transducer, enabling accurate correlation of the middle-sagittal NIR imaging plane with the sagittal US imaging.

The completed trans-rectal NIR/US probe and imager are shown in Fig. 2. The US probe was a bi-plane sector and linear array trans-rectal probe fitted to an ALOKA SSD-900V unit. The NIR applicator was integrated over the 7.5 MHz sagittal-imaging transducer. The NIR probe consisted of one source and one detector array separated 20 mm laterally and placed symmetrically to the sagittal US transducer. The NIR source and detector array, each having seven channels, were 60 mm in longitudinal dimension, which was identical to the longitudinal length of the sagittal US transducer. Each NIR optode channel had a micro prism-lens pair for coupling the light to and from the probe surface. The NIR light from a super-luminescent diode of 100 mW at 840 nm was focused sequentially onto seven source fibers of the NIR applicator by a home-made translating fiber multiplexer. The NIR remissions collected by the seven detection fibers were acquired by a 16-bit intensified CCD camera through a spectrometer (not necessary for acquiring the data but used for system integrity). Acquisition of NIR signals from seven source channels took less than five seconds after the prostate was localized by the sagittal US using an Aloka SSD-900V portable US scanner, which provides 50 mm longitudinal field of view when performing sagittal imaging with the 60 mm long 7.5 MHz US transducer. The absorption and reduced scattering coefficients of the prostate were reconstructed from steady-state measurements²² using a model-based non-linear optimization method.^{22,25,26} The effective attenuation coefficient is then calculated based on Eq. (1).

Table 2. Optical properties of normal canine prostate tissue as reported in various published studies. N is the number of samples. This table follows the template for human prostate in Ref. 24.

Study [Ref.]	Year	Sample	N	Method	λ (nm)	μ_a (mm^{-1})	μ'_s (mm^{-1})	μ_{eff} (mm^{-1})
Oraevsky <i>et al.</i> [12]	1997	<i>In vitro</i>	2		355	0.852	5.22	3.94
Oraevsky <i>et al.</i> [12]	1997	<i>In vitro</i>	2		532	0.233	2.45	1.37
Chen <i>et al.</i> [13]	1997	<i>In vivo</i>	17		630	0.04 ± 0.02	2.6 ± 2.1	0.5 ± 0.1
Chen <i>et al.</i> [13]	1997	<i>Ex vivo</i>	10		630	0.030 ± 0.007	2.6 ± 0.8	0.48 ± 0.09
Lee <i>et al.</i> [14]	1997	<i>In vivo</i>	7		630			0.47 ± 0.05
Nau <i>et al.</i> [15]	1999	<i>In vitro</i> (fresh)	10		633	0.073 ± 0.007	0.225 ± 0.005	$0.256 \pm 0.015^*$
Nau <i>et al.</i> [15]	1999	<i>In vitro</i> (frozen)	13		633	0.076 ± 0.003	1.00 ± 0.11	$0.495 \pm 0.027^*$
Lilge <i>et al.</i> [16]^	2004	<i>In vivo</i>	7		660	0.0030 ± 0.0021	0.92 ± 0.65	$0.184 \pm 0.040^\wedge$
Lilge <i>et al.</i> [16]^	2004	<i>In vivo</i>	7	Capsule 	660	0.0014 ± 0.0013	3.23 ± 2.76	$0.206 \pm 0.035^\wedge$
Jankun <i>et al.</i> [17]	2004	<i>In vivo</i>	13	Urethra 	665			0.171 ± 0.071
Jankun <i>et al.</i> [17]	2004	<i>In vivo</i>	13	Capsule 	665			0.192 ± 0.027
Jankun <i>et al.</i> [17]	2004	<i>In vivo</i>	13	Urethra 	665			0.259 ± 0.193
Jankun <i>et al.</i> [17]	2004	<i>In vivo</i>	13	Capsular base 	665			0.275 ± 0.131
Jankun <i>et al.</i> [17]	2004	<i>In vivo</i>	13	Urethral base 	665			$0.176 \pm 0.031^\wedge^\wedge$
Jankun <i>et al.</i> [17]~	2004	<i>In vivo</i>	13	Capsular apex 	665			0.190 ± 0.065
Jankun <i>et al.</i> [17]	2004	<i>In vivo</i>	13	Urethral apex 	665			0.247 ± 0.06
Jankun <i>et al.</i> [18]	2005	<i>In vivo</i>	5	Base 	665			0.203 ± 0.026
Jankun <i>et al.</i> [18]	2005	<i>In vivo</i>	5	Apex 	665			
Solonenko <i>et al.</i> [19]	2002	<i>In vivo</i>	4		730		1.27 ± 0.06	
Zhu <i>et al.</i> [20]	2003	<i>In vivo</i>	12		732	0.003–0.058	0.1–2.0	0.03–0.49
Nau <i>et al.</i> [15]	1999	<i>In vitro</i> (fresh)	7		1064	0.027 ± 0.003	1.76 ± 0.13	$0.381 \pm 0.026^*$
Nau <i>et al.</i> [15]	1999	<i>In vitro</i> (frozen)	10		1064	0.071 ± 0.006	0.79 ± 0.05	$0.428 \pm 0.023^*$
Oraevsky <i>et al.</i> [12]	1997	<i>In vitro</i>	2		1064	0.009	0.63	0.13

Note: *Calculation of the effective attenuation coefficient based on Eqs. (1) and (2).

^The values in the abstract of Ref. 16 are contrary to those in the text of Ref. 16. The results in the text were used here.

^^The results given in Ref. 17 were “ $0.176 \pm 0.314 \text{ mm}^{-1}$,” which had the standard deviation larger than the mean value. The authors made a “reasonable” estimation of “ $0.176 \pm 0.0314 \text{ mm}^{-1}$ ” for this set of literature data.

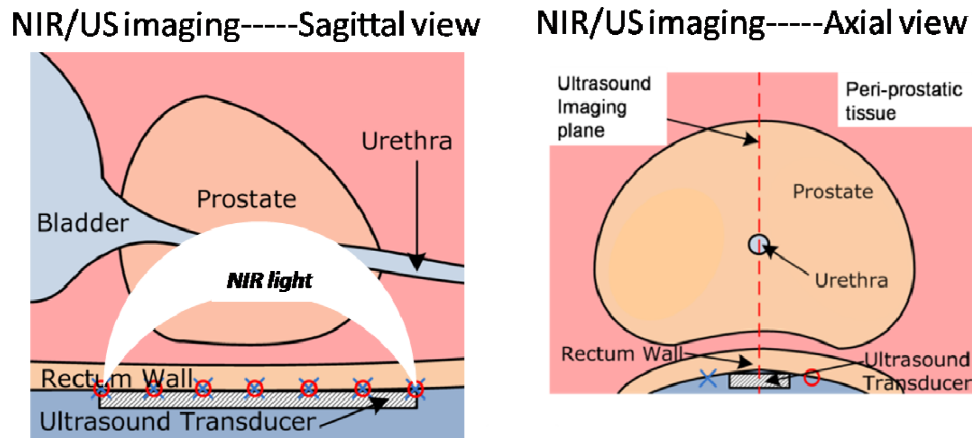


Fig. 1. Illustration of trans-rectal NIR/US of the prostate. Trans-rectal US is placed in the middle of the trans-rectal NIR applicator (optodes distributed longitudinally) to perform combined and correlated NIR/US imaging of the prostate at the sagittal plane.

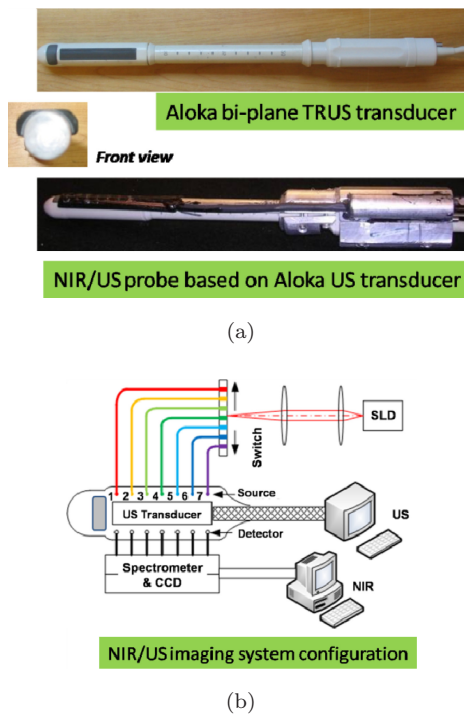


Fig. 2. (a) Photograph of the trans-rectal Aloka US transducer and the completed NIR/US probe. (b) Schematic diagram of the trans-rectal NIR/US imaging system that consists of a custom-built NIR imager and a commercial ALOKA SSD-900V portable US scanner.

3.2. Sensitivity features of the trans-rectal NIR imaging

Since the purpose of this study was to examine the inherent NIR contrast that the prostate may demonstrate over the peri-prostatic tissue, the NIR image was reconstructed without any spatial *prior* information. The accuracy or the robustness of the

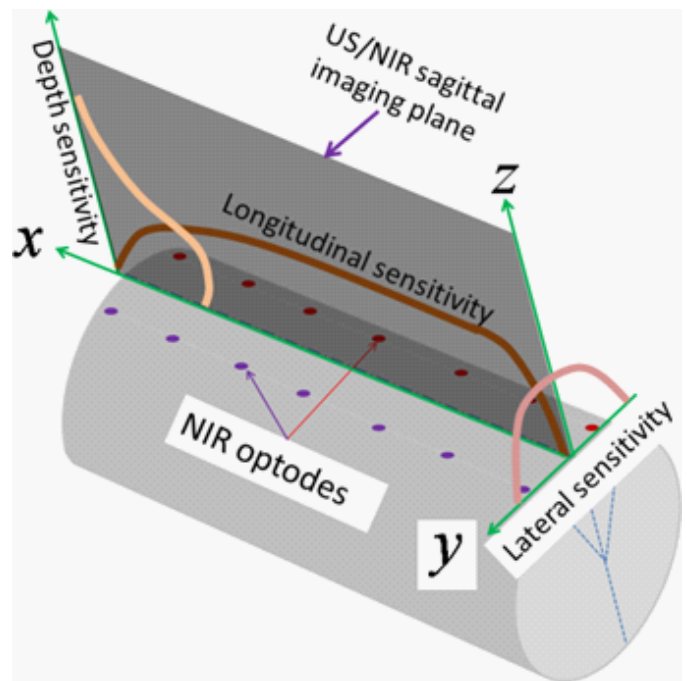


Fig. 3. Sensitivity profiles of the NIR imaging probe along the lateral, longitudinal and depth directions.

NIR reconstruction is thereby dependent upon the sensitivity of NIR array to the heterogeneity of the optical properties within the volume being interrogated. Figure 3 illustrate the sensitivity profiles, with respect to the absorption, of the NIR applicator based on the previous study.²¹ The longitudinal sensitivity is relatively uniform over the entire NIR array dimension, but it tapers off at the distal and proximal edges of the NIR array. The lateral sensitivity peaks at the middle-sagittal plane that coincides with the sagittal TRUS plane, while the

depth sensitivity generally degrades along with the increase of the depth. The sensitivity to the scattering or total attenuation would have similar patterns. Based on these sensitivity features, one could expect that a target may be reconstructed with better contrast if it is located within the regions of higher NIR sensitivity. It is also anticipated that for multiple targets located longitudinally on the same sagittal plane, the contrast-comparison would be reliable.

3.3. Animal model

This study was approved by the Institutional Animal Care and Use Committee of Oklahoma State University. The protocol was also approved and underwent an on-site inspection by the US Army Medical Research and Materiel Command. A 20-kg sexually intact, adult mixed-breed dog, approximately four years of age, was anesthetized using an intravenous injection of propofol (8 mg/kg) followed by intubation and halothane/oxygen inhalation for anesthetic maintenance. The animal was placed in left lateral recumbency for bowel preparation and physical examination (rectal palpation) of the prostate. TRUS visualization was performed using the combined trans-rectal NIR/US probe with condom-and-gel coverage. Both the physical examination and ultrasound revealed a normal prostate for this dog. The prostate was examined weekly using similar procedures, with consistent evaluation results being classified as “normal,” until the dog was euthanized nine weeks after the initial exam with an overdose of pentobarbital sodium. A complete necropsy was performed and the prostate and peri-prostatic structures were submitted for histologic examination.

4. Results

Figure 4 displays one set of sagittal trans-rectal NIR tomography images and the correlated TRUS performed at the right lobe, middle-line, and the left lobe of the normal canine prostate gland. The dimensions of the NIR and correlated TRUS images are 50 mm (cranial-to-caudal) \times 30 mm (dorsal-to-ventral). Each of the images represents one of three highly consistent measurements taken at each location.

The NIR absorption coefficient images are displayed at a color-scale of [0.007 0.014] mm^{-1} . The NIR transport scattering coefficient images are displayed at a color-scale of [3.000 6.000] mm^{-1} . The

NIR effective attenuation coefficient images are displayed at a color-scale of [0.250 0.500] mm^{-1} . The color-scales in all images represent a background threshold at $1/2$ of the maximum value of the color-scale. At this scale, the locations of the NIR regions indicating the prostate had excellent position correlation with prostatic images obtained using TRUS. The urinary bladder is shown as an anechoic structure on TRUS, which is similar to images using NIR. Most of the peri-rectal tissues are also not identified using NIR except at the periphery of the urinary bladder. The prostate is consistently demonstrated in NIR images as having positive-contrast with respect to the peri-prostatic tissues, with an average of more than two-folds of contrast in absorption, reduced scattering, and effective attenuation. In addition, the prostate is more optically heterogeneous in the middle-line and more optically attenuating toward the internal aspects of the prostate than in the peripheral aspects of the gland.

At this scale setting, it is noted that areas of prostatic regions on NIR images resemble the actual cross-sections being interrogated on the gland. The cranial-caudal length dimensions of the prostate at the right lobe and left lobe NIR images are smaller than that at the middle-line NIR images. The dorsal-ventral thickness dimensions of the prostate in the right and left lobe NIR images are shown greater than that at the middle-line NIR images. Overall, the prostate is longitudinally elongated in the middle line than in the right and left lobes. This profile of the canine prostate interpreted from NIR regions implies a walnut-shape with lobular anatomy.

Figure 4 illustrates peak absorption coefficients of this prostate specimen on the three planes to be 0.014, 0.012, and 0.014 mm^{-1} ; the peak reduced scattering coefficients to be 5.28, 5.56, and 6.53 mm^{-1} ; and the peak effective attenuation coefficients to be 0.45, 0.43, and 0.50 mm^{-1} . The validity of these numbers has been examined in the context of values summarized in Table 2 and by the spectra plots in Fig. 5. The majority of the previous measurements in Table 2 were performed in the spectral range of 630 nm to 732 nm, with some extension to the ultraviolet end of 355 nm and the infrared end of 1064 nm. The data points of this study, performed at 840 nm, represent the values of absorption, reduced scattering, and effective attenuation averaged over the peak values of right lobe, middle line, and left lobe. It is noted that the absorption coefficients of this study are

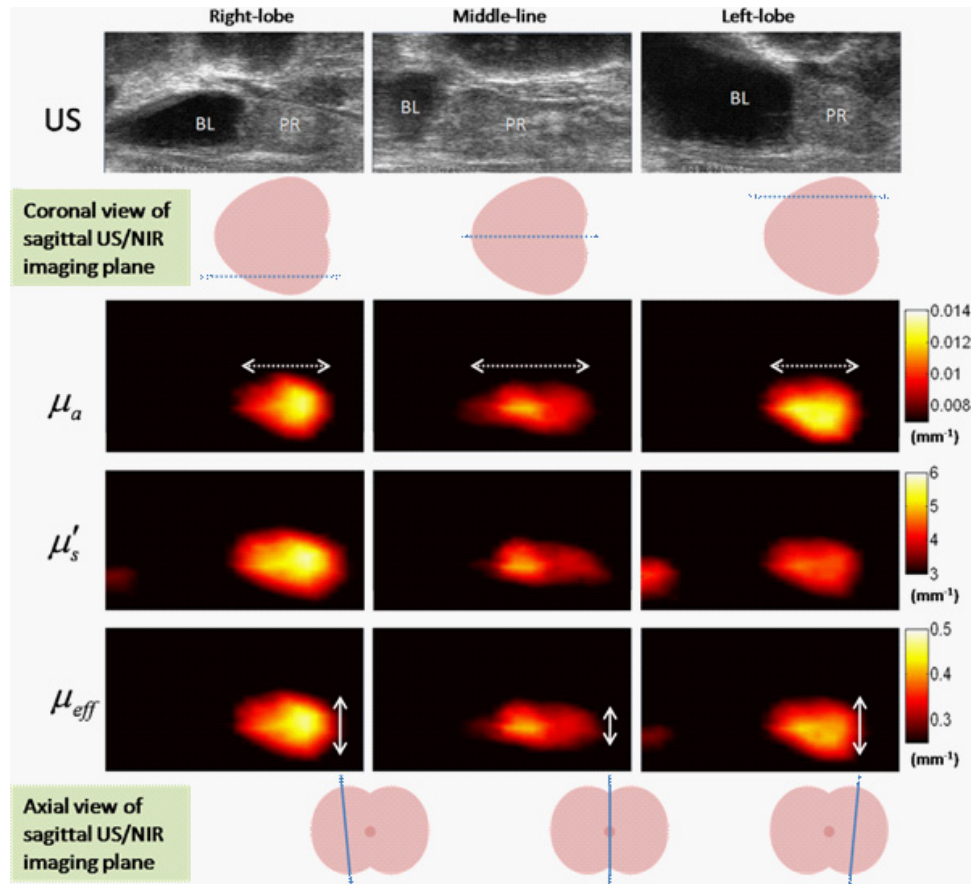


Fig. 4. Trans-rectal NIR/US of normal canine prostate *in vivo*: The US and NIR images were taken at the right lobe (left column), middle-line (middle column), and the left lobe (right column). The 1st row, US; the 2nd row, coronal view of the locations of sagittal NIR/US planes; the 3rd row, absorption coefficient; the 4th row, transport scattering coefficient; the 5th row, effective attenuation coefficient; the 6th row, axial view of the locations of sagittal NIR/US planes. The dimensions of all images are 50 mm × 30 mm (cranial-caudal × dorsal-ventral). BL-urinary bladder, PR-prostate.

narrowly distributed in a range predicted by the reported values closest to 840 nm. The reduced scattering values of this study are much higher (2–3 folds) than what may be estimated from the previously reported values, yet the effective attenuation coefficients of this study are narrowly distributed within the range predictable by reported values.

5. Gross and Histological Examination of the Prostate Gland

The prostate gland exhibited diffuse, symmetrical (and mild) enlargement (4.5 cm × 4.5 cm × 2.5 cm). On cross-section, the tissue was grossly normal with the exception of a discrete, 0.5 cm in diameter focus of grey/tan tissue [arrowhead, Fig. 6(b)] located in the region of the right prostatic lobe. Histologically, this focus corresponded to moderate interstitial

fibrosis with infiltration by primarily lymphocytic inflammatory cells [arrow, Fig. 6(d)]. The remainder of the prostatic tissue exhibited diffuse slight enlargement of the prostatic epithelium with occasional papillary projections and cystic dilation of prostatic glands consistent with early benign prostatic hyperplasia/hypertrophy. Otherwise, the tissue was histologically unremarkable [Fig. 6(c)]. The histological results confirmed that the NIR optical contrasts presented in this work are of a normal canine prostate.

6. Discussions

This study revealed the *in vivo* optical properties of an intact normal canine prostate in its normal anatomic position in the pelvic canal. The absorption, reduced scattering and effective attenuation coefficients of the canine prostate at approximately 840 nm have not been reported previously. However,

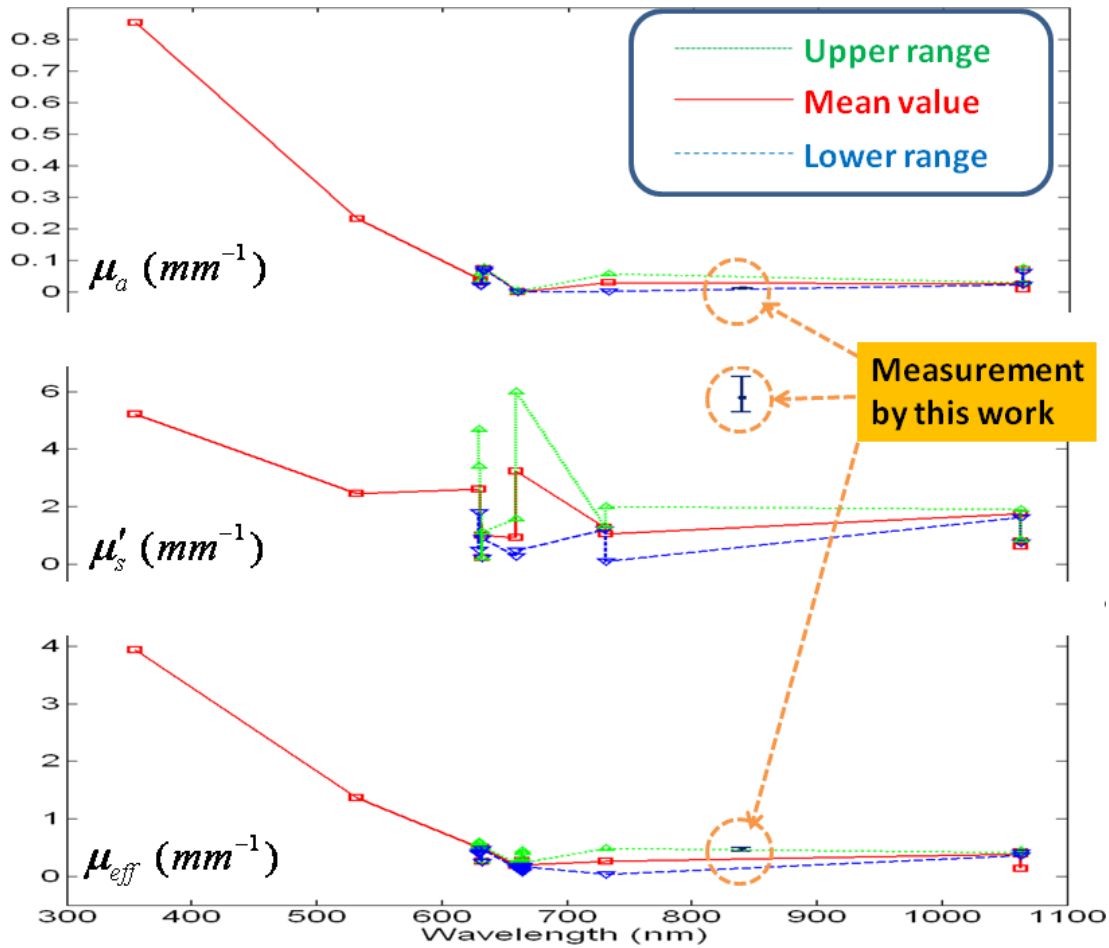


Fig. 5. Spectra of the optical properties of canine prostate based on the values given in Table 2. The measurements by this work at 840 nm were the average of the peak values of the right lobe, middle line, and left lobe.

an examination of the spectra in Fig. 5 allowed estimation of these values to be around that value. Given that the prostate is a gland with relatively rich vasculature, it is not difficult to correlate the absorption spectrum of the prostate to that of the total hemoglobin content, which has a low NIR absorption at and above the near-infrared band, as well as a relatively leveled absorption at wavelengths greater than the isosbestic point of 805 nm. The reduced scattering spectrum is rather “noisy” in the NIR band, yet globally it seems to follow the empirical power-law model of $\mu'_s = A\lambda^{-b}$, where A and b are model parameters for scattering amplitude and scattering power, respectively,²⁷ when there is a broad range of scattering particle sizes. The effective attenuation spectrum is close to that of the absorption, a result that may be anticipated from Eq. (1). Among the three optical properties being measured or calculated, both the absorption and effective attenuation coefficients are well within what can be predicted from the current literature.

The predicted average reduced scattering values at 840 nm from the literature may be much smaller than the measured values in this study but there is a fairly large error of distribution within the cited values of the spectra. It is thereby impractical to predict the reduced scattering coefficient at 840 nm within a narrow range based on the literature spectra. On the other hand, this study utilized non-*prior* guided pure optical-based reconstruction for trans-rectal optical tomography. Our previous study indicated that when an accurate spatial *prior* to trans-rectal NIR tomography reconstruction is not employed, the absorption coefficients may be under-estimated, and the reduced scattering coefficients may be over-estimated.²¹ The image reconstruction of trans-rectal NIR tomography in this study requires a 3D mesh being used due to the geometry of the NIR applicator. Extracting an accurate 3D prostate profile based on sagittal TRUS images, however, remains a challenging task. If the optical properties were reconstructed with an accu-

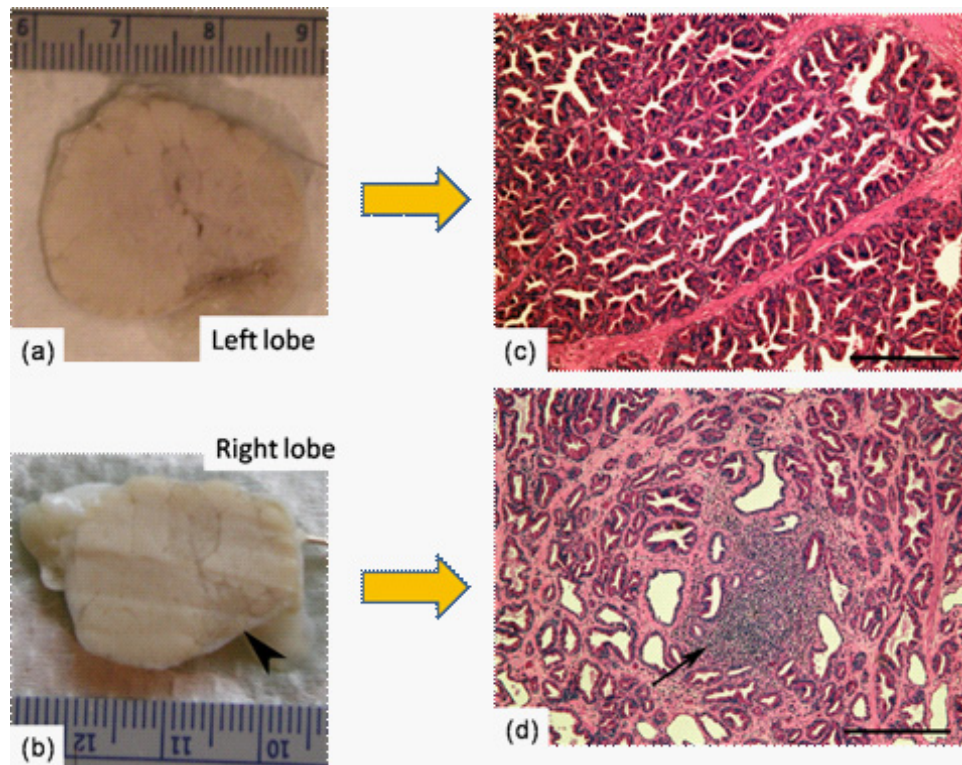


Fig. 6. Canine prostate gland. The prostate gland was slightly enlarged ($4.5\text{ cm} \times 4.5\text{ cm} \times 2.5\text{ cm}$) and on cross-section was predominantly unremarkable (a). The right lobe of the prostate contained a 0.5-cm in diameter focus of grey/tan tissue [arrowhead in (b)]. Histologically, most of the prostate gland exhibited inconspicuous lesions of early prostatic hyperplasia/hypertrophy consisting of increased prostatic epithelial cell size (c), scattered papillary projections and cystic dilation of prostatic acini. The gross lesion in the right prostatic lobe consisted of a focus of interstitial fibrosis and lymphocytic prostatitis [arrow in (d)]. Hematoxylin and Eosin stain, Bar = $360\ \mu\text{m}$.

rate spatial *prior*, the reduced scattering coefficients could have better correlation with the literature predictions.

This study also revealed the optical property contrasts that a normal canine prostate has over other structures within the canine pelvic canal. The prostate is shown as having positive-contrast over its peripheral tissue in absorption, reduced scattering, and effective attenuation of the NIR light. There are a number of factors that could make the prostate hyper-attenuating on trans-rectal NIR tomography. First, the unique thin-layers of prostatic capsule may be refractive-index mismatched with respect to the peri-prostatic tissue, thereby causing specular reflection on the prostatic capsule that contributes to the elevated light attenuation of the prostate. Second, the prostate is known to have relatively rich vasculature that may impose stronger NIR absorption within the prostate. Third, the intra-prostatic parenchyma is known to be optically heterogeneous,^{12–20} a condition favorable to high scattering attenuation. The origin of the

intra-prostatic optical heterogeneity is not well understood, but is likely due to multiple factors. These factors may include (1) the radially-distributed blood vessels giving non-uniform blood vessel count throughout the prostate, (2) the unique intra-prostatic anatomy that is complicated by the existence of urethra and ejaculation ducts, and (3) the different cellular structures in the different zonal areas of the prostate. Among these factors, the first and second may also cause the higher effective attenuation in the urethral region than in the capsular region that is clearly demonstrated in Refs. 15 and 16.

7. Conclusions

In conclusion, the optical properties of a normal canine prostate, *in vivo*, in its native intact environment in pelvic canal have been acquired for the first time by trans-rectal NIR optical tomography at 840 nm, under TRUS position-correlation but with

no spatial *prior* employed in the reconstruction. The absorption and effective attenuation coefficients are within the ranges predictable at 840 nm by literature values which clustered sparsely from 355 nm to 1064 nm. The effective attenuation coefficients are found higher in the internal aspects of the prostate than in the peripheral aspects, which agrees with the previous findings that the urethral regions were statistically more attenuating than the capsular regions.

Acknowledgment

This work has been supported by the Prostate Cancer Research Program of the US Army Medical Research Acquisition Activity (USAMRAA), 820 Chandler Street, Fort Detrick, MD, 21702-5014, through a Grant #W81XWH-07-1-0247.

References

- Q. Chen, Z. Huang, D. Luck, J. Beckers, P. H. Brun, B. C. Wilson, A. Scherz, Y. Salomon, F. W. Hetzel, "Preclinical studies in normal canine prostate of a novel palladium-bacteriopheophorbide (WST09) photosensitizer for photodynamic therapy of prostate cancers," *Photochem. Photobiol.* **76**, 438–445 (2002).
- K. K. Wang, L. Lutzke, L. Borkenhagen, W. Westra, M. W. Song, G. Prasad, N. S. Buttar, "Photodynamic therapy for Barrett's esophagus: Does light still have a role?" *Endoscopy* **40**, 1021–1025 (2008).
- J. B. Wang, L. X. Liu, "Use of photodynamic therapy in malignant lesions of stomach, bile duct, pancreas, colon and rectum," *Hepatogastroenterology* **54**, 718–724 (2007).
- M. A. D'Hallewin, D. Kochetkov, Y. Viry-Babel, A. Leroux, E. Werkmeister, D. Dumas, S. Gräfe, V. Zorin, F. Guillemain, L. Bezdetnaya, "Photodynamic therapy with intratumoral administration of lipid-based mTHPC in a model of breast cancer recurrence," *Lasers Surg. Med.* **40**, 543–549 (2008).
- B. J. Tromberg, J. Coquoz, O. Fishkin, J. B. Pham, T. Anderson, E. R. Butler, J. Cahn, M. Gross, J. D. Venugopalan, D. Pham, "Non-invasive measurements of breast tissue optical properties using frequency-domain photon migration," *Phil. Trans. R. Soc. Lond. B* **352**, 661–668 (1997).
- B. W. Pogue, S. P. Poplack, T. O. McBride, W. A. Wells, K. S. Osterman, U. L. Osterberg, K. D. Paulsen, "Quantitative hemoglobin tomography with diffuse near-infrared spectroscopy: Pilot results in the breast," *Radiology* **218**, 261–266 (2001).
- V. Ntziachristos, B. Chance, "Probing physiology and molecular function using optical imaging: Applications to breast cancer," *Breast Cancer Res.* **3**, 41–46 (2001).
- R. Choe, A. Corlu, K. Lee, T. Durduran, S. D. Konecky, M. Grosicka-Koptyra, S. R. Arridge, B. J. Czerniecki, D. L. Fraker, A. DeMichele, B. Chance, M. A. Rosen, A. G. Yodh, "Diffuse optical tomography of breast cancer during neoadjuvant chemotherapy: A case study with comparison to MRI," *Med. Phys.* **32**, 1128–1139 (2005).
- M. A. Franceschini, K. T. Moesta, S. Fantini, G. Gaida, E. Gratton, H. Jess, W. W. Mantulin, M. Seeber, P. M. Schlag, M. Kaschke, "Frequency-domain techniques enhance optical mammography: Initial clinical results," *Proc. Nat. Acad. Sci. USA* **94**, 6468–6473 (1997).
- Q. Zhu, E. B. Cronin, A. A. Currier, H. S. Vine, M. Huang, N. Chen, C. Xu, "Benign versus malignant breast masses: Optical differentiation with US-guided optical imaging reconstruction," *Radiology* **237**, 57–66 (2005).
- H. M. Ross, J. A. Smelstoys, G. J. Davis, A. S. Kapatkin, F. Del Piero, E. Reineke, H. Wang, T. C. Zhu, T. M. Busch, A. G. Yodh, S. M. Hahn, "Photodynamic therapy with motexafin lutetium for rectal cancer: A preclinical model in the dog," *J. Surg. Res.* **135**, 323–330 (2006).
- A. A. Oraevsky, S. L. Jacques, F. K. Tittel, "Measurement of tissue optical properties by time-resolved detection of laser-induced transient stress," *Appl. Opt.* **36**, 402–415 (1997).
- Q. Chen, B. C. Wilson, S. D. Shetty, M. S. Patterson, J. C. Cerny, F. W. Hetzel, "Changes in *in vivo* optical properties and light distributions in normal canine prostate during photodynamic therapy," *Radiat. Res.* **147**, 86–91 (1997).
- L. K. Lee, C. Whitehurst, Q. Chen, M. L. Pantelides, F. W. Hetzel, J. V. Moore, "Interstitial photodynamic therapy in the canine prostate," *Br. J. Urol.* **80**, 898–902 (1997).
- W. H. Nau, R. J. Roselli, D. F. Milam, "Measurement of thermal effects on the optical properties of prostate tissue at wavelengths of 1,064 and 633 nm," *Lasers Surg. Med.* **24**, 38–47 (1999).
- L. Lilge, N. Pomerleau-Dalcourt, A. Douplik, S. H. Selman, R. W. Keck, M. Szkudlarek, M. Pestka, J. Jankun, "Transperineal *in vivo* fluence-rate dosimetry in the canine prostate during SnET2-mediated PDT," *Phys. Med. Biol.* **49**, 3209–3225 (2004).
- J. Jankun, L. Lilge, A. Douplik, R. W. Keck, M. Pestka, M. Szkudlarek, P. J. Stevens, R. J. Lee, S. H. Selman, "Optical characteristics of the canine prostate at 665 nm sensitized with tin etiopurpurin dichloride: Need for real-time monitoring of photodynamic therapy," *J. Urol.* **172**, 739–743 (2004).

18. J. Jankun, R. W. Keck, E. Skrzypczak-Jankun, L. Lilge, S. H. Selman, "Diverse optical characteristic of the prostate and light delivery system: Implications for computer modelling of prostatic photodynamic therapy," *B. J. U. Int.* **95**, 1237–1244 (2005).
19. M. Solonenko, R. Cheung, T. M. Busch, A. Kachur, G. M. Griffin, T. Vulcan, T. C. Zhu, H. W. Wang, S. M. Hahn, A. G. Yodh, "In vivo reflectance measurement of optical properties, blood oxygenation and motexafin lutetium uptake in canine large bowels, kidneys and prostates," *Phys. Med. Biol.* **47**, 857–873 (2002).
20. T. C. Zhu, S. M. Hahn, A. S. Kapatkin, A. Dimofte, C. E. Rodriguez, T. G. Vulcan, E. Glatstein, R. A. Hsi, "In vivo optical properties of normal canine prostate at 732 nm using motexafin lutetium-mediated photodynamic therapy," *Photochem. Photobiol.* **77**, 81–88 (2003).
21. G. Xu, D. Piao, C. H. Musgrove, C. F. Bunting, H. Dehghani, "Trans-rectal ultrasound-coupled near-infrared optical tomography of the prostate Part I: Simulation," *Opt. Exp.* **16**, 17484–17504 (2008).
22. Z. Jiang, D. Piao, G. Xu, J. W. Ritchey, G. R. Holyoak, K. E. Bartels, C. F. Bunting, G. Slobodov, J. S. Krasinski, "Trans-rectal ultrasound-coupled near-infrared optical tomography of the prostate Part II: Experimental demonstration," *Opt. Exp.* **16**, 17505–17520 (2008).
23. J. Boutet, L. Guyon, M. Debourdeau, J. M. Dinten, D. Vray, P. Rizo, "Advances in bi-modal optical and ultrasound detection of prostate cancer diagnosis," *Proc. SPIE* **7171**, 71710E (2009).
24. T. Svensson, S. Andersson-Engels, M. Einarsdóttir, K. Svanberg, "In vivo optical characterization of human prostate tissue using near-infrared time-resolved spectroscopy," *J. Biomed. Opt.* **12**, 014022 (2007).
25. N. Iftimia, H. Jiang, "Quantitative optical image reconstruction of turbid media by use of direct-current measurements," *Appl. Opt.* **39**, 5256–5261 (2000).
26. H. Xu, *MRI-Coupled Broadband Near-Infrared Tomography for Small Animal Brain Studies*, Ph.D. Dissertation, Dartmouth College, Hanover, NH, p. 36 (2005).
27. F. Bevilacqua, A. J. Berger, A. E. Cerussi, D. Jakubowski, B. J. Tromberg, "Broadband absorption spectroscopy in turbid media by combined frequency-domain and steady-state methods," *Appl. Opt.* **39**, 6498–6510 (2000).